Materials Advances

ROYAL SOCIETY OF CHEMISTRY

PAPER

Published on 26 October 2026
Licensed under CC-BY 4.0

Check for updates

Cite this: DOI: 10.1039/d6ma01090c

Atomic-scale insights into the origin of lithium metal anode nucleation heterogeneity

Matthias J. Golomb,†[af] Ali Nasrallah,†[af] Neubi F. Xavier,[a] Emilia Olsson,[bc] Cheng Hu,[d] James Robinson[ef] and Qiong Cai*[af]

Received 20th July 2026,
Accepted 25th October 2026

DOI: 10.1039/d6ma01090c

rsc.li/materials-advances

The development of high-performance rechargeable batteries is critical for the future of energy storage, with lithium metal anodes offering a promising avenue due to their high theoretical capacity and low electrochemical potential. However, lithium dendrite formation compromises their safety and cyclability. While classical nucleation theory explains growth at the mesoscale, the atomic-scale mechanisms governing lithium nucleation remain less understood. This study employs periodic density functional theory (DFT) simulations to investigate the early-stage nucleation of lithium atoms on lithium metal Li(100), Li(110) and Li(111) surfaces. Following the determination of pristine surface energetics and preferred adsorption sites, the analysis is extended to the effect of surface defects, such as oxygen, nitrogen, and fluorine, which commonly arise from interactions with manufacturing atmospheres and battery electrolytes. The findings of this study reveal that defect chemistry significantly alters nucleation behaviour, with fluorine defects acting as persistent nucleation seed sites which could promote uniform growth under sufficient concentration on the surface. These insights provide a fundamental understanding of lithium nucleation at the atomic level and suggest strategies for surface and electrolyte engineering to mitigate dendrite formation, ultimately contributing to the design of safer and more efficient lithium metal batteries.

1. Introduction

The accessibility of affordable, reliable, and sustainable energy is one of the central topics of current research, and consequently also part of the sustainable development goals of the United Nations.[1] While the implementation of renewable energy has grown rapidly over the last years, one of the main challenges to overcome is the electrification of key sectors such as automotive and aerospace. Rechargeable batteries are one of the main technologies used in this regard, with lithium-ion batteries (LIBs) at the forefront of current adoption. Current Li-ion cells, which deploy a graphite based negative electrode, offer compelling energy densities for passenger automotive vehicles, but efforts to move beyond this are hampered by the theoretical capacity limit of 372 mAh g^{-1} with graphite. Attempts to overcome this limit have included the study of alloying type electrodes including silicon, which can yield significantly higher capacities, though suffer from severe volume expansion with high degrees of lithiation.[2] While current generations of battery cells are competitive to fossil fuels, improvements in energy density and safety are crucial for commercial success. An alternative improvement to the incumbent graphite negative electrode is the use of Li metal instead: this has gathered increasing attention due to its lightweight nature (0.59 g cm^{-3}), high theoretical specific capacity (3860 mA h g^{-1}), and low negative electrochemical potential.[3] Alongside the so-called Li-metal batteries, which replace graphite in LIBs with Li metal as the anode material, other battery systems such as Li–O_2, Li–CO_2, and Li–sulfur batteries also use Li metal anodes and have been considered as promising candidates.[4] Despite the high energy density promises of the above-mentioned batteries utilising Li metal anodes, two main challenges pose an obstacle in their commercialization: (1) potential safety risks associated with Li dendrite growth during the charge/discharge process, and (2) low coulombic efficiency as a result of undesired reactions of Li metal anode and electrolyte.[5]

During the charging process in these systems, Li metal is deposited onto the negative electrode surface. This process has

[a] School of Chemistry and Chemical Engineering, Faculty of Engineering and Physical Sciences, University of Surrey, Guilford GU2 7XH, UK. E-mail: q.cai@surrey.ac.uk
[b] Institute for Theoretical Physics, University of Amsterdam, Science Park 904, Amsterdam, 1098 XH, The Netherlands
[c] Advanced Research Center for Nanolithography, Science Park 106, Amsterdam, 1098 XG, The Netherlands
[d] Key Laboratory for Liquid–Solid Structural Evolution and Processing of Materials (Ministry of Education), School of Materials Science and Engineering, Shandong University, Jinan, Shandong 250061, P. R. China
[e] Department of Chemical Engineering, Electrochemical Innovation Lab, University College London, London WC1E 7JE, UK
[f] The Faraday Institution, Quad One, Bequerel Avenue, Research Complex at Harwell Didcot, Oxfordshire OXYZ 123, UK
† These authors contributed equally to this work.

© 2026 The Author(s). Published by the Royal Society of Chemistry

been widely shown to be non-uniform across multiple length scales, causing the flux of lithium ions to vary locally on the surface of the anode.[6] This can result in the formation of dendrites, branch-like structures growing on top of the anode surface,[7] which can damage the existing solid electrolyte interface (SEI), the protective layer that arises when the electrolyte reacts with the metal anode and necessitate the formation of new SEI when fresh Li is exposed to the electrolyte. This causes severe phase migrations, electrolyte depletion, and heat accumulation.[8] Moreover, as these dendrites grow and deplete during cycling, their interaction with the SEI can lead to parts of the dendrite breaking off the anode surface, causing the formation of ''dead Li'', Li which no longer participates in the operation of the battery.[9] As a result, the coulombic efficiency of the cell drops as more dead lithium is produced, causing the battery to operate inefficiently. Furthermore, uninhibited dendrite growth can lead to a puncture of the separator, creating an internal short circuit and accelerating the end of life of the cell or worse, inducing thermal failure.[10] While the exact formation process and composition of the SEI is a topic of ongoing research, its main constituents using standard electrolytes are thought to be Li_2O, Li_2CO_3, LiF, Li_3N and ROCOO-Li where R represents different alkyl structures.[11] It is therefore reasonable to assume that the interaction of the anode and the SEI will introduce certain defects that are derived from these constituents. However, very little work has so far been done on defect engineering in lithium metal anodes, such as the beneficial effect of the introduction of zinc and silver defects on the uniformity of lithium deposition *via* a reduction of its nucleation potential.[12]

The process of dendrite growth can be described as a two-stage process: Li nucleation and Li growth. Work performed by Ely and Garcia first investigated the heterogeneous nucleation process based on classical nucleation theory, which establishes growth conditions based on the size of a deposit (also called embryo) on a surface and the applied overpotential.[13] In their work, they identified five different regimes that are part of the dendrite formation process: nucleation suppression, long incubation time, short incubation time, early growth, and late growth. In the first regime, embryo size and overpotential are too small to lead to growth, and the deposit dissolves into the electrolyte. In the second regime, small overpotentials allow for the embryos to remain metastable, but do not effectively grow in size. Above a critical overpotential, the short incubation time regime begins where very narrow size distributions of nuclei occur. Finally, in the last two phases, thermodynamically and kinetically stable nuclei grow at steady rates.

This growth behaviour has been observed in numerous studies, under different conditions.[14,15] Transmission X-ray microscopy (TXM) and cryo transmission electron microscopy (TEM) have also been used as experimental tools to observe the post mortem Li dendrite and SEI after the deposition and stripping processes, at the micrometre length scale,[14,16] and recently even up to nanometre scale.[17] *In situ* optical microscopy has been used to observe the process of Li growth in real-time to understand how voltage variations during the charge/discharge process can affect the morphology of the dendrites.[18] It however remains a challenge to enable both high resolution at atomic or nanometer scale and *in operando* conditions for experimental imaging techniques that would be required to study early nucleation phenomena. In addition, electron irradiation used for *in situ* techniques can degrade the liquid electrolyte and promote dendrite formation, which makes it difficult to draw unambiguous conclusions from their results.[19]

Computationally, models based on classical nucleation theory and mathematical models have been developed to understand the nucleation process.[20] A recently published study for example examined the nucleation of Li metal on different surfaces using kinetic Monte Carlo simulations based on classical nucleation theory.[21] In this model, a pre-existing cluster of Li adatoms is introduced as an embryo for further nucleation. In their study, Jiao *et al.* found that nuclei with a radius of 52 nm have a very low confidence probability of 10% to stabilize and are thus likely to dissolve. Bigger clusters in the range of 98 nm had a higher confidence probability and thus had higher chance to grow. In recent years the mesoscale evolution of dendrites has also been addressed using the phase-field method, which treats the electrode/electrolyte interface *via* a diffuse order parameter and couples it with Li^+ transport, electric potential (or overpotential), and even mechanics or thermal fields. Phase-field models allow simulation of morphological evolution of the metal deposit (branching, competition among nuclei, tip growth, dissolution) under varying overpotential, ion-flux heterogeneity and interface mobility. For example, early work by Hong & Viswanathan[22] used a grand-potential phase-field model to show the transition from smooth to dendritic growth when ion-transport becomes limiting. Subsequent studies have extended this framework to include effects of separator thickness & coating as well as the interplay of temperature and overpotential.[23]

While the above studies provide insight into dendrite growth at the mesoscale, it implies the existence of embryos at the anode surface. The formation of these embryos itself however happens at the atomic scale, which makes the characterization and description of this initial growth step challenging. Experimentally, the required atomic resolution, femtosecond timescales for initial Li deposition and dynamic nature of the lithiation process render most characterization techniques unsuitable. This necessitates the use of modelling and simulation; however, little work has been undertaken to examine the nucleation process of Li on the Li metal anode in batteries. Selis *et al.* studied the growth of dendritic structures on the Li metal anode using classical molecular dynamics (MD) simulations, showing that existing LiF cracks in the SEI lead to the formation of pillar structures.[24] Gaissmaier *et al.* investigated the adsorption and diffusion of single atoms on the low-index surfaces of Li and Na metal, revealing differences in early-stage nucleation on different facets.[25] Nagy *et al.* investigated the deposition of metal atoms on metal surfaces using density functional theory (DFT) simulations, predicting body-centered cubic surfaces to allow for high nucleation rates.[26] In a recent study, Bhandari *et al.* utilised linear-scale DFT to study Li nucleation on a graphite anode under an applied

© 2026 The Author(s). Published by the Royal Society of Chemistry

potential, accurately reproducing experimental values for cluster growth potentials.[27] Li *et al.* shed light on the importance of surface chemistry using a combination of DFT and AIMD applied to graphene surfaces, showing that defects can have great impact on nucleation barriers without altering transport and desolvation.[28] No simulation studies have been performed to investigate the embryo stage of Li nucleation on different Li metal facets.

In this study, we employ periodic DFT first principles simulations to examine the early steps of nucleation of Li atoms on Li metal surfaces of varying surface chemistry. This leads to the identification of different early-stage nucleation scenarios based on the Li metal surface chemistry, opening potential avenues for improving nucleation behaviour on Li metal anodes through anode and electrolyte engineering.

2. Methods

Fig. 1 illustrates the overall workflow of the methodology we undertake. Initially, the energetics of the low-index Li metal surfaces (100), (110), (111) and (211) were calculated (see Fig. 1a). Bulk values for the initialization of surfaces were taken from the lowest energy structures for Li from the Materials Project.[29] Values for comparison of adsorption energetics on Cu facets were established analogously. Afterwards we compared the continuous adsorption of single Li atoms (Fig. 1b) as well as the adsorption of small tetrahedron Li clusters (Fig. 1c) on the three energetically most favourable lithium metal surfaces by sampling possible configurations of Li adatoms. The high symmetry sites chosen were top (situated directly above a Li atom of the topmost layer), bridge (situated in the interstitial space halfway between two topmost layer Li atoms), and hollow (situated in the interstitial space between two diagonally opposed Li atoms of the topmost layer) (see also Fig. 3a). Different initial rotations of the Li tetrahedron cluster on the surfaces were investigated but were found to have no effect on the resulting final structure. We then investigated the adsorption behaviour of Li in the presence of surface defects of oxygen, nitrogen, and fluorine as examples of defects arising from an interaction with common battery electrolytes (Fig. 1d). All simulations were carried out based on plane wave, periodic supercell, spin-polarized DFT calculations using the Vienna *Ab initio* Simulation Package (VASP),[30,31] version 6.5.1, using the projector augmented wave treatment of core–valence interactions[32] with the vdW-DF3-opt1 nonlocal density functional[33] for the exchange–correlation energy and vdW interactions[34,35] which has been shown to avoid the lattice-expansion errors of earlier vdW functionals while retaining the non-local dispersion forces missing in standard PBE. Energy cutoffs were chosen as 500 eV and a *k*-point mesh of $3 \times 3 \times 1$ was used after convergence tests on Li surfaces, and self-consistent-field electronic energies were converged to 10^{-5} eV and atomic forces to less than 0.01 eV $Å^{-1}$. Surfaces were constructed using pymatgen,[36] and checked for convergence in vacuum distance, after which a minimum vacuum distance of 10 Å was chosen for all calculations. The energetics of different surface indexes for lithium were established according to eqn (1).

$$E_{\text{surf}}^{\text{hkl}} = \frac{1}{2}\left(\frac{E_{\text{slab}}^{\text{hkl}} - E_{\text{bulk}}^{\text{hkl}} \times n_{\text{slab}}}{A_{\text{slab}}}\right) \quad (1)$$

where E_{surf}^{hkl} is the energy of a surface of index (*hkl*), E_{slab}^{hkl} is the total energy of a slab model calculated *via* DFT, E_{bulk}^{hkl} is the total energy per atom of a bulk DFT calculation, and n_{slab} and A_{slab} are the number of atoms and the surface area of the slab.[37] All models used six surface layers. To minimize the effect of periodic boundary conditions on defects in repeating cells, 3×3 supercells were used for calculations on pristine Li and Cu surfaces (see Fig. 1a) and 4×4 supercells for calculations including defects (see Fig. 1d). These were determined to be sufficient by comparison to a calculation of 5×5 supercells, where the per atom energy differed by less than 1%. Calculations of adsorption sites as well as defect structures were performed in analogy to the ShakeNBreak[38] code: after manual determination of symmetry inequivalent sites, small random displacements to the atoms in the structure of varying length were applied to break symmetry. These were subsequently relaxed, and the lowest energy adsorption/defect site were identified. Adsorption energies E_{ads} were calculated according to eqn (2).

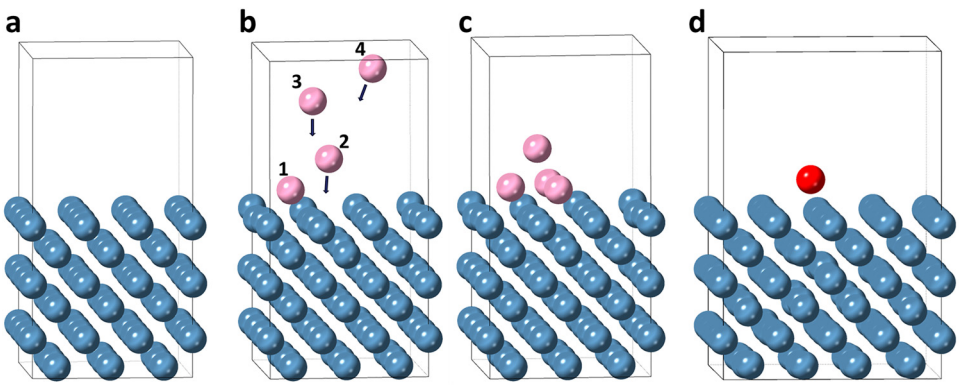


Fig. 1 Examples of initial geometries on the Li(100) facet for (a) the determination of surface energetics, (b) continuous adsorption of single Li atoms, (c) Li tetrahedron cluster adsorption and (d) Li adsorption on defective surfaces (oxygen in red is shown as an example).

© 2026 The Author(s). Published by the Royal Society of Chemistry

$$E_{ads} = [E_{x@surf} - (E_x + E_{surf})] \quad (2)$$

where E_x, E_{surf} and $E_{x@surf}$ are the energies of the adsorbed species/structure (taken from a vacuum reference calculation in a cubic box of 10 Å side length), the energy of the pristine surface and the energy of the surface with adsorbed structure, respectively. Nudged elastic band (NEB) calculations for the estimation of surface diffusion barriers were also performed in VASP, with six images along the pathway between symmetry inequivalent surface sites. Bader charge analysis of the defects was carried out using the code by the Henkelmann group.[39]

3. Results

3.1. Determination of lithium metal surface energetics

The low-index Li surfaces (100), (110) and (111) as well as (211) were investigated due to literature reports of dendritic growth on these facets.[8] The surface energy describes the energy needed to form a surface of a certain direction in a crystal, and a lower energy of formation is preferred. In our calculations, Li(100) and Li(110) turn out to be highly competitive with lower surface energy (0.53 Jm^{-2} and 0.51 Jm^{-2}), whereas Li(111) and Li(211) are significantly less favourable with higher surface energy (0.63 Jm^{-2} and 0.62 Jm^{-2}). These values agree well with the experimental value of $\sim$0.5 Jm^{-2}.[40] The resulting Wulff construction is shown in Fig. 2, giving a visual indication of the ideal equilibrium shape of a free crystallite as the set of points $\boldsymbol{x}$ satisfying

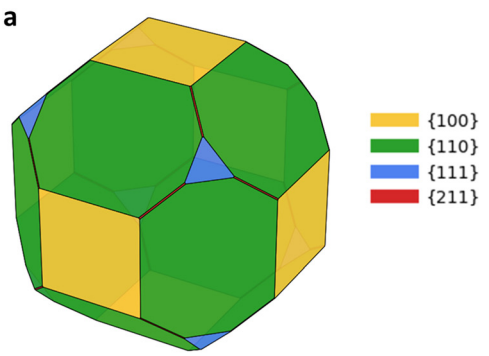
$$W = \{\boldsymbol{x}:\boldsymbol{x} \times \boldsymbol{n} \leq \gamma[\boldsymbol{n}]\forall \boldsymbol{n}\}$$

where $\boldsymbol{n}$ denote all directions and $\gamma[\boldsymbol{n}]$ is the associated direction-dependent surface energy.[41] This motivated further investigation of the low index surfaces, while an investigation of the (211) surface was not pursued due to its low formation probability and inhibitive computational cost.

3.2. Nucleation of Li atoms on pristine lithium surfaces

An overview of the simulation results for a single Li atom adsorption calculation on the three different facets Li(100), Li(110) and Li(111) is given in Fig. 3. Since any physical system tries to minimize its total energy, adsorption energies that lead to stable structures are negative, and lower negative values are energetically preferred. For the Li(100) facet, the hollow site was found to be more energetically favoured than the top and bridge sites, with an adsorption energy of −1.29 eV. Adsorption at this site leads to no noticeable surface reconstruction, as it follows the underlying AB layer stacking pattern. This result is also in agreement with previously published work by Gaissmaier *et al.*[42] For the (111) facet, the favourable one Li atom adsorption site is found closest to the bridge site with an adsorption energy of −1.62 eV following the underlying stacking pattern. For the (110) facet, the top site is the favoured adsorption site with an adsorption energy of −1.39 eV; however, the adsorption does not follow the expected underlying AB layer stacking pattern but leads to minor surface reconstruction. This might be a result of the closer surface plane packing of the (110) facet compared to the other facets, prohibiting adsorption at hollow or bridge sites. While these results come from calculations performed at 0 K, one can estimate the influence of temperature by considering the average thermal energy at room temperature, k_BT = 25 meV. For the Li(100) facet, neither the top nor bridge site adsorption energy lies in this thermal energy window of 25 meV above the ground state. Consequently, the hollow site remains the only accessible adsorption site even with this temperature approximation. For Li(110) and Li(111) however, respectively the bridge (E_{ads} = −1.37 eV) and top (E_{ads} = −1.60 eV) sites could be thermally accessible. Based on the adsorption energies of Li at the most favourable site on the three Li facets, one can stipulate that Li adsorption on the (110) and (111) facets would be more favoured compared to (100), leading to preferential adsorption of Li on Li(110) and Li(111) if all three facets are present. This is in agreement with experimentally observed lower overpotential for Li nucleation on the Li(110) facet compared to (100) in the work by Zhao *et al.*,[43] which will be discussed further below.

To study the effect of continued deposition of lithium, calculations of adsorption energies with additional Li atoms were performed on all facets. These calculations were initialized based on the resulting minimum energy configuration of the previous adsorption step, *i.e.* from the hollow site adsorption configuration for the (100) facet, the top site for the (110) facet, and the bridge site for the (111) facet. Similar to the first



b

Surface	Surface Energy J m^{-2} vdW-DF3-opt1
Li(100)	0.53
Li(110)	0.51
Li(211)	0.62
Experimental	0.50

Fig. 2 (a) Wulff construction of Li metal and (b) corresponding values and experimental results showing the surface energies associated with different Li planes within a Li crystallite with clear favourability toward the formation of the Li(100) and Li(110) planes in the crystallite due to a lower surface energy.

© 2026 The Author(s). Published by the Royal Society of Chemistry

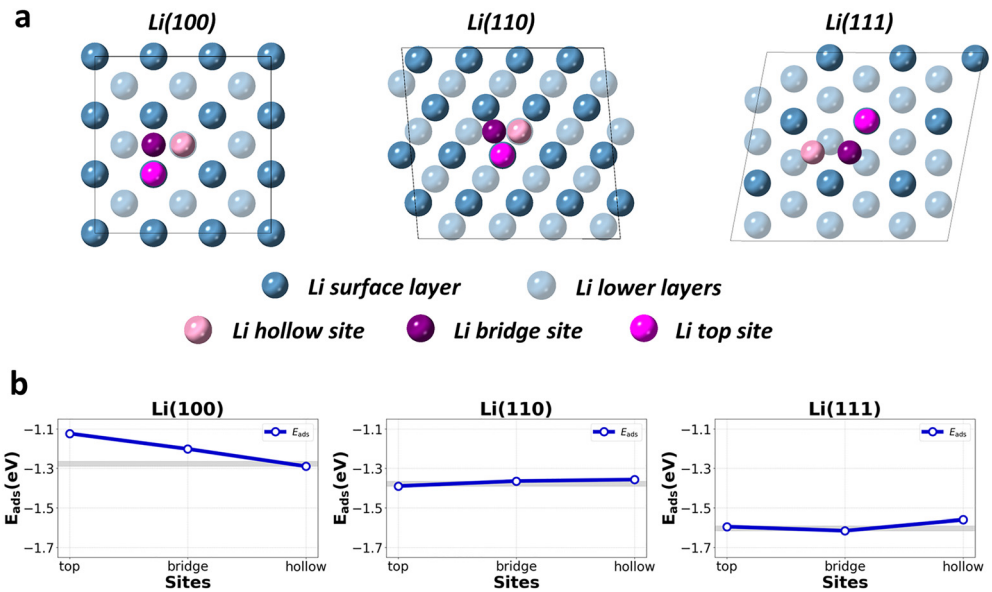


Fig. 3 (a) Top view of the initial sites considered for surface adsorption on the Li(100), Li(110) and Li(111) facets. Solid blue beads represent Li atoms of the topmost layer, whereas transparent blue beads represent the Li atoms of the second layer. Pink, pastel and purple beads represent top, hollow and bridge sites. (b) Adsorption site energies on Li(100), (110) and (111) facets, with the energy window for k_BT at room temperature shaded in grey to visualize potential thermal effects.

single atom adsorption, top, bridge and hollow configurations of these new starting structures were sampled. On the (100) facet, continued deposition followed the regular stacking pattern, with additional atoms occupying hollow sites, leading to uniform coverage of the surface with Li adatoms (see Fig. 4a). Adsorption energies for additional Li atoms at symmetry inequivalent site closest to the prior adsorption site were found to be lower than pristine surface adsorption energies, such as −1.50 eV for the adsorption of a second Li atom on Li(100), *vs.* −1.29 eV for one single Li atom adsorption. This indicates that growth from a nucleation seed is energetically preferred over simultaneous uniform adsorption on the pristine surface. This is confirmed by the calculation of the adsorption energy away from the initial adsorption site, which we found to reproduce the result of a simple single Li atom adsorption (E_{ads} = −1.29 eV). For the (111) surface, a behaviour similar to the (100) surface is obtained, where continuous adsorption follows the underlying stacking pattern leading to uniform deposition of Li on the bridge sites (Fig. 4c). Generally, adsorption on Li(111) is almost 200 meV stronger compared to Li(100) and Li(110) (*ca.* −1.5 eV on Li(111) compared to *ca.* −1.3 eV on Li(100/110)). While any Li crystallite is less likely to form the Li(111) facet naturally due to its high formation energy compared to the Li(100)/Li(110) facets, it is possible for the latter to expose this surface at certain grain boundaries where its cleavage changes. At these grain boundary facets, the stronger adsorption energies of Li(111) facets could lead to preferential adsorption over the grain surface itself, explaining proposed growth mechanisms of insertion at grain boundaries.[44] Interestingly, continued deposition of Li atoms on the (110) facet remained to be top-site favoured up until the third atom, leading to extended surface reconstruction (see Fig. 4b). The fourth atom however adsorbs favourably on the hollow site of the triangle of Li atoms adsorbed beforehand. This could potentially be attributed to the energy minimization of the maximally close packed cluster on the (110) surface, while a similar structure on the (100) facet is not close packed.

Cluster calculations were then initialized with four Li atoms in a tetrahedron arrangement as the smallest three-dimensional adsorbing structure. On the (100) and the (111) facets, Li tetrahedron clusters prove to be unstable and relax into structures occupying the next layer of the surface, in agreement with the calculations of the previous section. We then performed additional constrained calculations to assess the possible formation of metastable[45] cluster states, in which the cluster atoms were only allowed to move along the *z*-direction. If metastable states are found, these could potentially serve as nucleation seeds in fast deposition scenarios before decomposition into simple layered structures, especially under the influence of an external potential accelerating the speed of deposition. On the (100) facet, the adsorption energy of the metastable Li_4 cluster was found to lie 60 meV above its corresponding minimum energy structures (−5.99 eV continuous adsorption *vs.* −5.93 eV cluster adsorption). In previous studies, an analysis of the existence of states above the convex hull minimum has shown that this is well within the range to be metastable.[46] While such cluster nucleation seeds can thus not be discarded as embryos for dendrite formation at fast timescales, they are unlikely to be one of the main nucleation seeds.

The adsorption of the Li_4 tetrahedron cluster on the (111) surface was less favourable than the continuous adsorption scenario (−6.52 eV continuous adsorption *vs.* −6.40 eV cluster adsorption), rendering these highly unlikely to exist under any deposition conditions. The scenario is different for the (110) facet, where Li clusters adsorbing as a single unit are found to be more

© 2026 The Author(s). Published by the Royal Society of Chemistry

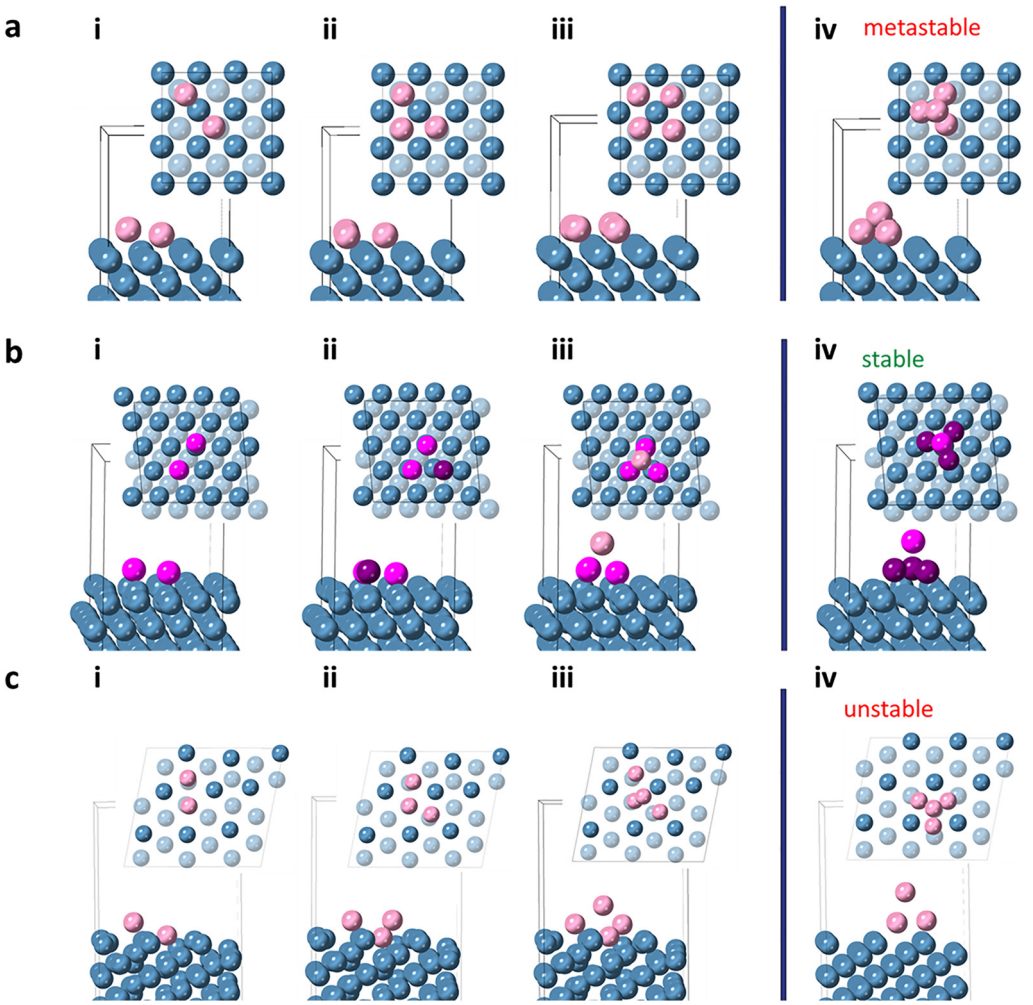


Fig. 4 Structures of continuous Li deposition for the (a) (100), (b) (110) and (c) (111) facet. The first three images (i–iii) in each row correspond to the adsorption of two, three and four Li atoms, respectively, while the last image (iv) is the resulting structure of the most stable constrained Li cluster calculation with which the probability of metastable states of multi-atom adsorbing structures can be assessed. For Li(100), continuous adsorption is favoured but clusters are metastable, for Li(110) clusters are stable and favoured over continuous adsorption, while for Li(111) continuous adsorption is favoured and clusters are unstable.

stable than its continuously grown counterpart (−4.90 eV continuous adsorption *vs.* −4.94 eV cluster adsorption), which could lead to non-uniform growth of Li clusters on this facet. It has to be noted however that this energy difference lies in the window of metastability, and additional effects such as temperature could make the uniform growth conditions accessible.

3.3. Li nucleation on defective surfaces

One of the crucial aspects of battery systems with a Li metal anode is the formation of the SEI which is a result of the interaction of the various components of the electrolyte with the Li metal anode. This layer is composed of a mixture of components associated with Li-reactivity with the electrolyte and serves to stabilise the Li-metal electrode. It is therefore reasonable to assume that a continued battery cycling process will introduce defects on the anode surface stemming from this Li metal-electrolyte interaction. Some of the most common SEI constituent compounds include Li_2O, LiF and Li_3N.[47] While a comprehensive investigation of non-idealized cells of these complexes with DFT on various Li metal surfaces and geometries such as grain boundaries or rough surfaces is desirable, they would result in very large supercells to avoid self-interaction across periodic images, making it computationally prohibitive. This motivates the study of single components of the complex species, namely oxygen (O), nitrogen (N), and fluorine (F) defects on the Li surface. It should be noted that in experiment not only these species are present on a commercially provided Li foil, but a supplier dependent native passivation layer which may introduce additional species beyond the scope of this study.

We started by examining the adsorption of a single heteroatom of O, N and F on the Li(100) surface. Initial positions were chosen as discussed earlier at hollow, bridge and top sites of the Li surface, with displacements applied before relaxation. Fig. 5 shows the results of the relaxation, with considerable differences for each defect. The most stable configuration for oxygen on the (100) facet is found to be a penetration of the

© 2026 The Author(s). Published by the Royal Society of Chemistry

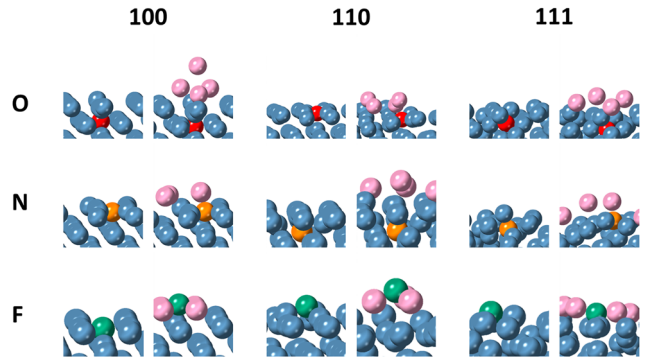


Fig. 5 Defect surfaces for oxygen, nitrogen and fluorine on the three Li metal facets (100), (110) and (111). Li atoms are shown in blue and O, N and F in red, orange and green, respectively. Adsorbed Li atoms are shown in pastel for clarity. For each facet and defect, the surface without lithium adatoms and after adsorption of four adatoms is shown. Contrary to oxygen and nitrogen, fluorine is not covered by lithium during the adsorption process.

oxygen atom into the surface, adopting octahedral coordination at an interstitial site in the second layer, consistent with the structure of lithium oxide. Nitrogen in comparison remains on the surface at a bridge site, whereas fluorine favourably adsorbs in an interstitial site within the top surface layer.

The different defects also show differences upon further lithiation, which was investigated by initializing additional Li atoms on symmetry inequivalent sites on top of and next to the defect site. We investigated this process up to four continuously adsorbed atoms to be able to compare the energetics to the adsorption of the four atom tetrahedron cluster. We will however focus our discussion on the cases of the first and second adatom: the comparison between these two cases is most informative of whether nucleation seeds will continue to grow, or whether the pristine adsorption away from the initial adsorption site is energetically favoured.

Generally, while both oxygen and nitrogen atoms are seemingly incorporated into the topmost Li(100) surface layer with additional Li atoms following the original stacking pattern with minimal lattice distortion, fluorine remains on top of the surface. A similar trend is observed for the other lowest-energy surfaces, where nitrogen and oxygen atoms assume interstitial sites upon continued Li deposition, leading to the eventual growth of pristine Li surfaces above the defect, while fluorine does not get covered. An explanation for this might be the electronegativity of fluorine, leading to stronger binding with Li atoms than oxygen and nitrogen, as also indicated by the shortest defect – Li distance in the pair distribution functions for the different facets (Fig. 6). This increases the barrier to move into a geometrically favoured interstitial site for fluorine. This continued accessibility might be another explanation for the improved cycling performances of lithium metal anode with LiF containing SEI.[48] The pair distributions of the different facets also reveal the buckling of Li metal atoms at the surface upon defect insertion, leading to distortions in the surface layers which are the most pronounced for the (111) surface. A Bader charge analysis of the different defect

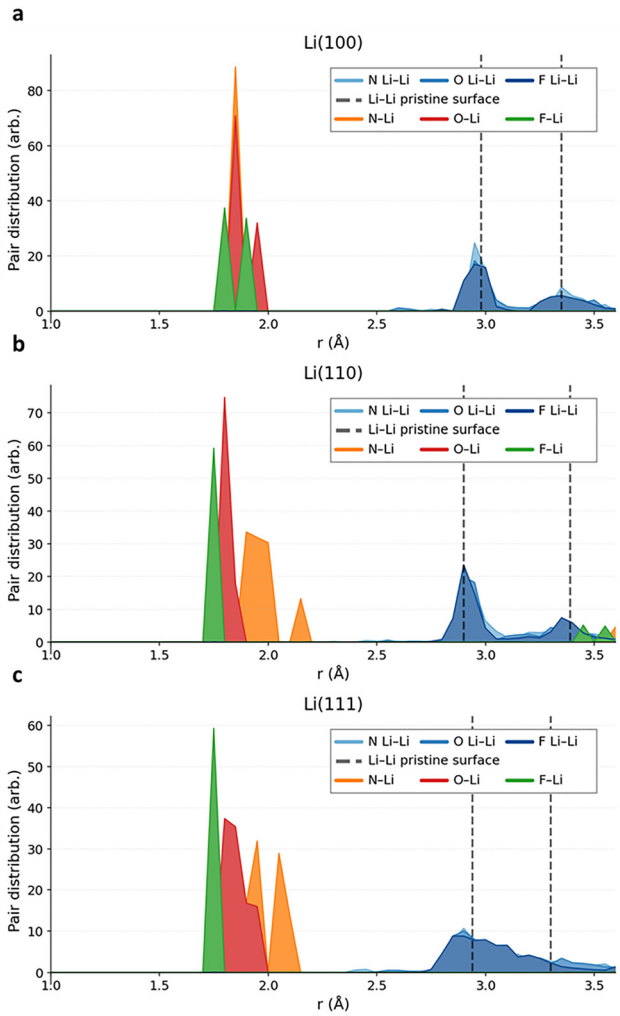


Fig. 6 Pair distribution functions of the defective surfaces (a) Li(100), (b) Li(110) and (c) Li(111) showing the crystal structure changes upon defect adsorption on the pristine surface. Dashed lines show the peak positions for the pristine surfaces. Li(111) shows the strongest distortion in the surface layers.

environments (see Fig. S1) found no significant difference between different facets and number of adatoms.

Energetically, the initial adsorption of Li on the (100) facet containing nitrogen (E_{ads} = −2.11 eV) and fluorine (E_{ads} = −1.40 eV) defect sites is strongly favoured (see Fig. 7 for all adsorption energies across different facets), whereas initial adsorption on the oxygen defect site (E_{ads} = −1.27 eV) is neither hindered nor facilitated compared to adsorption on the pristine surface which has almost the same adsorption energy (E_{ads} = −1.29 eV). This would lead to preferential growth on the nitrogen and fluorine defect sites on a Li(100) surface, leading to the formation of nucleation seeds and potentially dendritic structures. The effect of continuous adsorption of single Li atoms however varies significantly between defect chemistries: the adsorption energy of two Li on the nitrogen defect site weakens, while it strengthens for both oxygen and fluorine. As a result of both the favourable initial adsorption and preferential growth on the Li(100) plane containing fluorine, it is clear that

© 2026 The Author(s). Published by the Royal Society of Chemistry

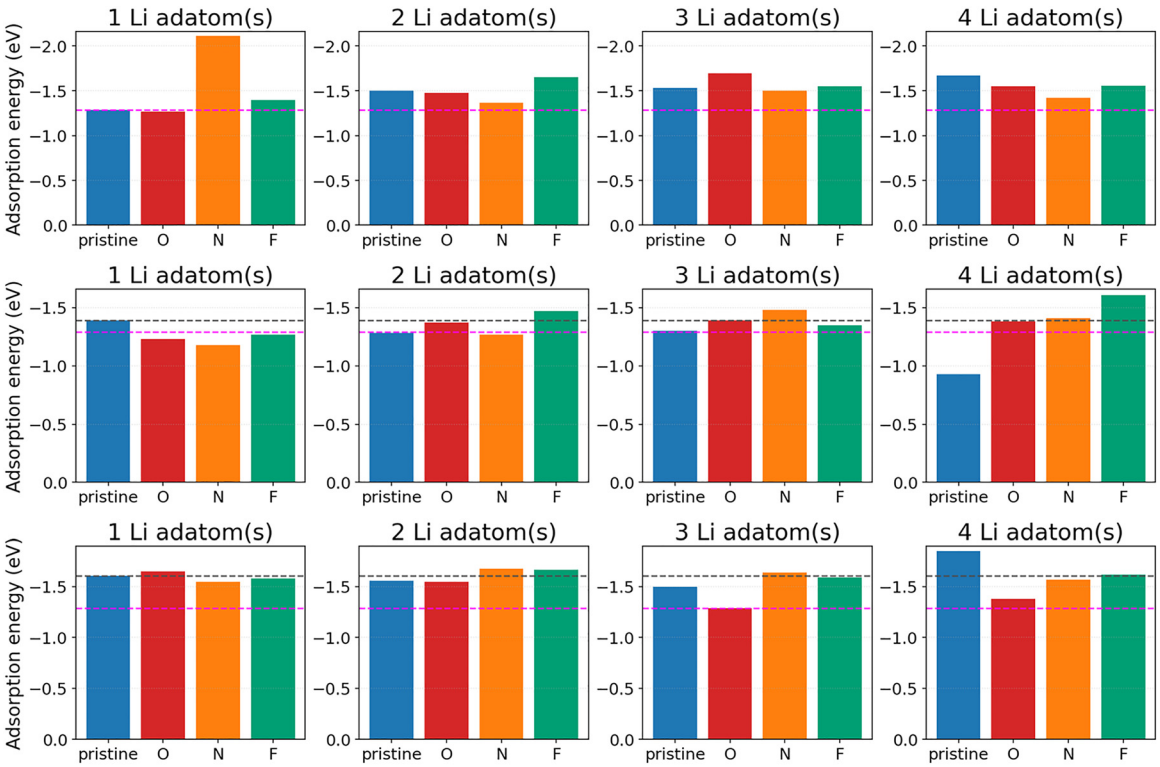


Fig. 7 Adsorption energies for the three studied Li anode surfaces: (100) (top row), (110) (middle row) and (111) (bottom row). Dashed pink lines are drawn at the Li(100) pristine surface adsorption energy for general reference, whereas grey dashed lines represent the adsorption energy of each pristine surface adsorption energy.

a fluorine defect would be the preferred growth sites for nucleation seeds over alternative oxygen or nitrogen sites.

For the Li(110) facet, initial single Li atom adsorption on defect sites (E_{ads} = −1.23 eV for the oxygen defect, E_{ads} = −1.18 eV for the nitrogen defect and E_{ads} = −1.27 eV for the fluorine defect) is energetically less favourable compared to the pristine adsorption on this facet (E_{ads} = −1.39 eV). Even under continuous single atom lithiation, only the fluorine defect site shows significantly stronger adsorption than the pristine counterpart (E_{ads} = −1.61 eV for the adsorption of the fourth Li adatom). The adsorption of one or two Li atom on the Li(110) surface containing oxygen or nitrogen defect is weaker compared to that containing fluorine defect, most likely due to the coverage of oxygen and nitrogen defects by lithium leading to a shielding effect of the defect site for adsorption (see Fig. 5).

For the Li(111) facet, no significant difference in adsorption energy is observed between the pristine surface and defective surfaces, except for much weaker adsorption on the oxygen defect site. A likely cause of this is the penetration of the oxygen defect into the surface and the subsequently shielded defect influence for oxygen, similar to the Li(110) facet behaviour, whereas nitrogen and fluorine do not penetrate the surface or get covered by adsorbed lithium atoms.

In addition to our investigation of continued single atom adsorption on the defect surfaces, we also investigated the adsorption of tetrahedron clusters consisting of four Li atoms, analogous to the procedure on pristine surfaces. Average adsorption energies per atom for these are shown in Fig. S2. We find none of these tetrahedron clusters to be stable at defect surfaces apart from the oxygen defect on the Li(100) facet, where a shortened distance between the defect and the surface Li atoms allows for a close packed cluster structure similar to the case of stable clusters on pristine Li(110).

While only static 0 K DFT adsorption energies are presented here, it is worth noting that nucleation behaviour in real systems is also influenced by kinetic factors such as surface diffusion barriers and adatom mobility. The relatively large differences of up to −1 eV in adsorption energies between facets and defect sites suggest corresponding variations in surface diffusion rates, which may govern the transition between uniform and dendritic growth. We thus performed nudged elastic band calculations to compare diffusion barriers to the various adsorption energies we obtained (Fig. 8a). The calculated barrier heights are in the range of ∼0.25 eV to ∼0.5 eV, comparable to other diffusion barriers calculated in the literature.[49] This is of the order of most adsorption energy differences found in the above analysis of thermodynamically preferred adsorption. It is therefore reasonable to assume that a significant adsorbing atom might overcome the kinetic barriers between different adsorption sites due to their difference in adsorption energy. This competition between thermodynamic preference and kinetic accessibility is therefore clearly of great importance to Li growth behaviour but remains beyond the scope of this paper. We thus recommend the use of

© 2026 The Author(s). Published by the Royal Society of Chemistry

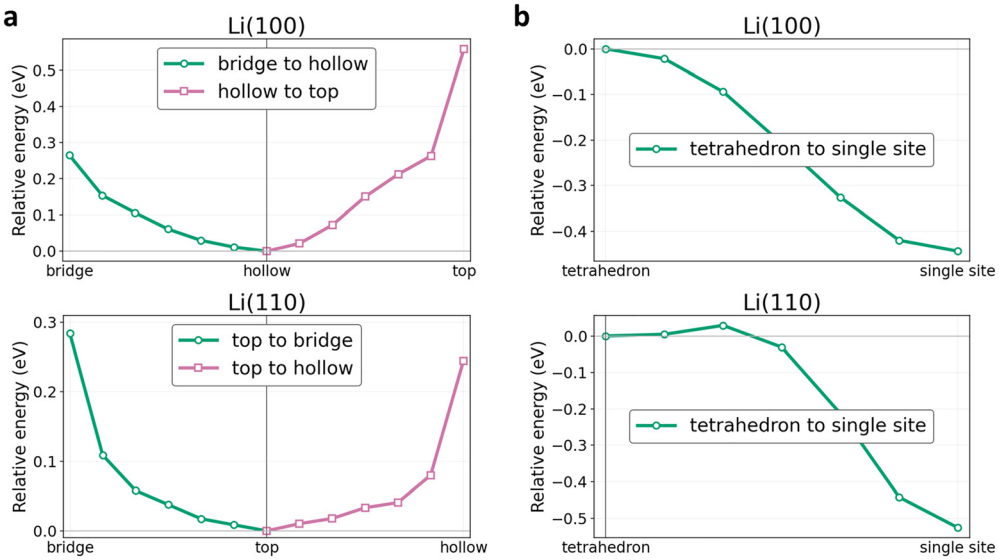


Fig. 8 Diffusion barriers for single lithium atoms between symmetry inequivalent surface sites on (a) Li(100) and (b) Li(110) calculated *via* nudged elastic band. The calculated barrier heights are of the same order of magnitude as the adsorption energy differences between different growth scenarios.

techniques incorporating dynamic effects such as *ab initio* molecular dynamics in future work. We also calculated the energy profile of a single Li atom on a trajectory from the top site of a tetrahedron arrangement to a pristine site away from the initial adsorption site. As expected, this process is barrierless on (100) but has a barrier of roughly 29 meV for the (110) facet.

3.4. Li adsorption growth scenarios

Based on the above results, it is possible to construct different adsorption scenarios on the Li metal anode, which we have schematically depicted in Fig. 9. On pristine Li(100) and Li(111) facets, Li adsorption is expected to intrinsically be uniform across the surfaces, spreading in the direction of the surface plane from initially adsorbed atoms (Fig. 9 top row). This type of growth can best be compared to mossy growth, as this would result in multiple lithium seeds growing at roughly equal speeds and eventually merging.[50] On Li(110), dendrites could form if lithium deposition is fast enough for single Li adatoms not to relax into their minimum energy positions, but to form more stable tetrahedron clusters instead. A similar process is possible on the (100) facet; however, since small Li clusters are at best metastable in this case, this would require an even greater speed of deposition.

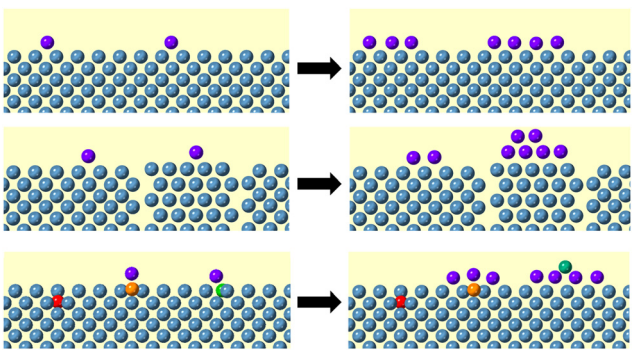


Fig. 9 Schematic of different growth scenarios based on this study. Top row: Growth scenario based on nucleation seeds on a pristine Li(100) surface, with Li-adatoms coloured in purple. Middle row: Growth scenario based on nucleation seeds on grains of Li(100) and Li(110) facets. Bottom row: Growth scenario based on nucleation seeds on a Li(100) surface including O (red), N (orange) and F (green) defects.

If different facets of Li are present (likely to be the case in a real battery), growth turns from a uniform to a non-uniform scenario. Since adsorption of single Li atoms on the Li(110) facet (E_{ads} = −1.39 eV) is favoured compared to the (100) facet (E_{ads} = −1.29 eV), this is likely to lead a greater accumulation of Li on the Li(110) facet due to energetic preference. Adsorption of single Li atoms is even stronger for Li(111) facets (E_{ads} = −1.61 eV), indicating that the presence of Li(111) facets could lead to favoured Li accumulation, although Li(111) facets are less likely to be formed, according to the Wulff construction in Fig. 1. For both Li(110) and Li(111) facets, the stronger Li adsorption of further Li atoms compared to the Li(100) facet could thus lead to dendrite formation on these two surfaces, where the size of these dendrites will depend on the grain size of varying facets (Fig. 9 middle row). Li(110) is also the only pristine facet on which Li clusters are stable, further increasing the likelihood of dendrite formation on this surface.

Lastly, the presence of surface defects will influence the adsorption of Li on the anode surface, with stark differences between these defects (Fig. 9 bottom row). Since oxygen defects penetrate the surface, their effect on the Li single atom adsorption energy compared to the pristine surface will taper off under continuous single Li atom adsorption, resulting in a 'self-healing' process: the defect is incorporated into the crystal structure without changes to the pristine structure in subsequent layers. While nitrogen shows very strong initial single Li

© 2026 The Author(s). Published by the Royal Society of Chemistry

atom adsorption on the Li(100) surface, it shows a similar shielding effect for subsequent Li atom adsorption where it is incorporated into the structure as an interstitial site. Contrary to this, fluorine shows strong adsorption for single Li atoms but does not favour an incorporation as a bulk interstitial and remains on the Li anode surface and thus shows strong adsorption energies for single Li atoms even for the fourth single Li atom adsorption. A uniform distribution of fluorine defects could thus serve as persisting nucleation seeds during continuous Li deposition, leading to uniform growth at low overpotentials and/or fast deposition times.

It should be noted that the present study focuses on static adsorption energetics and does not explicitly include finite-temperature dynamics or solvent effects. These simplifications are deliberate to isolate intrinsic surface–defect interactions on Li metal. While they limit direct prediction of absolute nucleation rates, the relative trends observed here remain robust indicators of how surface chemistry governs early-stage Li growth. Future work may incorporate dynamic simulations or continuum-scale coupling to capture these effects quantitatively.

4. Conclusions

In this study, we employed periodic DFT simulations to investigate the early nucleation stages of lithium atoms on lithium metal surfaces with varying surface chemistries. Our results indicate that lithium adsorption on pristine Li(100) and Li(111) surfaces follows the expected stacking patterns, resulting in a growth scenario similar to what is experimentally known as 'mossy' growth, while cluster adsorption leading to non-uniform growth is energetically favoured for Li(110). Both the (110) as well as the (111) facet demonstrate preferential adsorption over (100), leading to dendrite formation based on the surface formation energetics due to formation of grains with different facets. The presence of surface defects, specifically oxygen, nitrogen, and fluorine, was found to significantly influence the nucleation behaviour. While oxygen and nitrogen defects were incorporated into the surface with minimal disruption, fluorine remained on the surface, acting as a persistent nucleation site. This suggests that controlled defect engineering, particularly fluorine incorporation, should be experimentally investigated to verify it as a potential strategy for enhancing uniform lithium deposition and mitigating dendrite growth in lithium metal anodes.[51] It should be noted that that these model findings explain underlying mechanisms of Li deposition but are influenced by a computationally intractable number of factors when operated in a real cell such as choice of solvent or preparation conditions. From an experimental standpoint it is thus instructive to consider which technique or component addresses the underlying problems outlined in this study best, such as *e.g.* the problem of surface heterogeneity can be dealt with for instance by either a cryogenic rolling strategy, a specific choice of solvent or using Li-alloys.

The implications of these findings extend to the optimization of lithium metal anodes for next-generation batteries. By tailoring surface properties and defect distributions, it may be possible to suppress dendritic growth, thereby enhancing the safety and efficiency of lithium metal batteries. The results in this study are obtained with conventional DFT calculations, which assumes various idealized conditions. While the inclusion of defects aims to simulate conditions more akin to real scenarios in one aspect, several other approximations should be investigated in the future to improve on the indications provided by computational models to realistic battery operation. Particularly, the inclusion of finite temperature, solvent/electrolyte and electrochemical potential effects will give valuable insights which can improve the inherent gap between computational models and real cells.

Conflicts of interest

There are no conflicts to declare.

Data availability

The data that support the findings of this study are available from the corresponding author upon reasonable request. The data needed to reproduce the findings of this study is publicly available in a Zenodo repository, *via* the following link: https://doi.org/10.5281/zenodo.23739923.

Supplementary information (SI): the supplementary information file contains the Bader charge and adsorption energy data on different Li facets. See DOI: https://doi.org/10.1039/d6ma01090c.

Acknowledgements

This work was supported by the Faraday Institution (https://www.faraday.ac.uk; EP/S003053/1) through the Lithium Sulfur Technology Accelerator (LiSTAR) programme (FIRG014, FIRG058, FIRG083). Funding support from the Royal Society (Grant No. IEC/NSFC/211200) and Horizon Europe *via* the OPERA consortium (grant no. 101103834) under the UK Research and Innovation (UKRI)'s Horizon Europe funding guarantee (grant no. 10078555) are also acknowledged. We are grateful to the UKMaterials and Molecular Modelling Hub for computational resources, which is partially funded by EPSRC (EP/T022213/1, EP/W032260/1 and EP/P020194/1). The Michael Supercomputer supported by the Faraday Institution (FIRG030) is also acknowledged for computational resources.

References

1 UNDESA. 2024. The Sustainable Development Goals Report 2024 – June 2024. NewYork, USA.
2 G. F. I. Toki, *et al.*, Recent progress and challenges in silicon-based anode materials for lithium-ion batteries, *Ind. Chem. Mater.*, 2024, **2**, 226–269.
3 W. Xu, *et al.*, Lithium metal anodes for rechargeable batteries, *Energy Env. Sci.*, 2014, **7**, 513–537.

© 2026 The Author(s). Published by the Royal Society of Chemistry

4 H. Raza, *et al.*, Li-S Batteries: Challenges, Achievements and Opportunities, *Electrochem. Energy Rev.*, 2023, **6**, 29.
5 Y. Zhang, *et al.*, Towards better Li metal anodes: Challenges and strategies, *Mater. Today*, 2020, **33**, 56–74.
6 R. E. Owen, *et al.*, Visualising the Effect of Areal Current Density on the Performance and Degradation of Lithium Sulfur Batteries Using Operando Optical Microscopy, *J. Electrochem. Soc.*, 2024, **171**, 120523.
7 B. Li, *et al.*, A Review of Solid Electrolyte Interphase (SEI) and Dendrite Formation in Lithium Batteries, *Electrochem. Energy Rev.*, 2023, **6**, 7.
8 X. Chen, B. Zhao, C. Yan and Q. Zhang, Review on Li Deposition in Working Batteries: From Nucleation to Early Growth, *Adv. Mater.*, 2021, **33**, 2004128.
9 Y. Li, *et al.*, Correlating Structure and Function of Battery Interphases at Atomic Resolution Using Cryoelectron Microscopy, *Joule*, 2018, **2**, 2167–2177.
10 C. Fang, *et al.*, Quantifying inactive lithium in lithium metal batteries, *Nature*, 2019, **572**, 511–515.
11 Z. Shen, *et al.*, Solid Electrolyte Interphase on Lithium Metal Anodes, *ChemSusChem*, 2024, **17**, e202301777.
12 S. Yang and D. Li, Alloying Strategies for Efficient Lithium–Metal Anodes: Bridging Phase Diagrams, Defect Engineering, and Interfacial Charge Redistribution, *Adv. Eng. Mater.*, 2026, **28**, e202501624.
13 D. R. Ely and R. E. García, Heterogeneous Nucleation and Growth of Lithium Electrodeposits on Negative Electrodes, *J. Electrochem. Soc.*, 2013, **160**, A662–A668.
14 J.-H. Cheng, *et al.*, Visualization of Lithium Plating and Stripping via *in Operando* Transmission X-ray Microscopy, *J. Phys. Chem. C*, 2017, **121**, 7761–7766.
15 A. Jana, S. I. Woo, K. S. N. Vikrant and R. E. García, Electrochemomechanics of lithium dendrite growth, *Energy Environ. Sci.*, 2019, **12**, 3595–3607.
16 Y. Li, *et al.*, Atomic structure of sensitive battery materials and interfaces revealed by cryo–electron microscopy, *Science*, 2017, **358**, 506–510.
17 B. Han, *et al.*, Poor Stability of Li_2CO_3 in the Solid Electrolyte Interphase of a Lithium-Metal Anode Revealed by Cryo-Electron Microscopy, *Adv. Mater.*, 2021, **33**, 2100404.
18 K. N. Wood, *et al.*, Dendrites and Pits: Untangling the Complex Behavior of Lithium Metal Anodes through Operando Video Microscopy, *ACS Cent. Sci.*, 2016, **2**, 790–801.
19 Y. Li, *et al.*, Visualizing Structure, Growth, and Dynamics of Li Dendrite in Batteries: From Atomic to Device Scales, *Adv. Funct. Mater.*, 2024, **34**, 2401361.
20 L. Chen, *et al.*, Modulation of dendritic patterns during electrodeposition: A nonlinear phase-field model, *J. Power Sources*, 2015, **300**, 376–385.
21 X. Jiao, *et al.*, Morphology evolution of electrodeposited lithium on metal substrates, *Energy Storage Mater.*, 2023, **61**, 102916.
22 Z. Hong and V. Viswanathan, Phase-Field Simulations of Lithium Dendrite Growth with Open-Source Software, *ACS Energy Lett.*, 2018, **3**, 1737–1743.
23 G. Qi, *et al.*, A three-dimensional multiphysics field coupled phase field model for lithium dendrite growth, *J. Energy Storage*, 2024, **101**, 113899.
24 L. A. Selis and J. M. Seminario, Dendrite formation in Li-metal anodes: an atomistic molecular dynamics study, *RSC Adv.*, 2019, **9**, 27835–27848.
25 D. Gaissmaier, M. Van Den Borg, D. Fantauzzi and T. Jacob, Microscopic Properties of Na and Li—A First Principle Study of Metal Battery Anode Materials, *ChemSusChem*, 2020, **13**, 771–783.
26 K. S. Nagy, S. Kazemiabnavi, K. Thornton and D. J. Siegel, Thermodynamic Overpotentials and Nucleation Rates for Electrodeposition on Metal Anodes, *ACS Appl. Mater. Interfaces*, 2019, **11**, 7954–7964.
27 A. Bhandari, *et al.*, Li nucleation on the graphite anode under potential control in Li-ion batteries, *J. Mater. Chem. A*, 2022, **10**, 11426–11436.
28 S. Li, B. Wang, T. W. Heo and M. Wood, Influence of surface chemistry on Li nucleation energetics on graphene-based surfaces, *J. Chem. Phys.*, 2025, **162**, 054703.
29 A. Jain, *et al.*, Commentary: The Materials Project: A materials genome approach to accelerating materials innovation, *APL Mater.*, 2013, **1**, 011002.
30 G. Kresse and J. Furthmüller, Efficiency of ab-initio total energy calculations for metals and semiconductors using a plane-wave basis set, *Comput. Mater. Sci.*, 1996, **6**, 15–50.
31 J. Furthmüller, J. Hafner and G. Kresse, Dimer reconstruction and electronic surface states on clean and hydrogenated diamond (100) surfaces, *Phys. Rev. B: Condens. Matter Mater. Phys.*, 1996, **53**, 7334–7351.
32 G. Kresse and D. Joubert, From ultrasoft pseudopotentials to the projector augmented-wave method, *Phys. Rev. B: Condens. Matter Mater. Phys.*, 1999, **59**, 1758–1775.
33 D. Chakraborty, K. Berland and T. Thonhauser, Next-Generation Nonlocal van der Waals Density Functional, *J. Chem. Theory Comput.*, 2020, **16**, 5893–5911.
34 J. Klimeš, D. R. Bowler and A. Michaelides, Chemical accuracy for the van der Waals density functional, *J. Phys.: Condens. Matter*, 2010, **22**, 022201.
35 J. Klimeš, D. R. Bowler and A. Michaelides, van der Waals density functionals applied to solids, *Phys. Rev. B: Condens. Matter Mater. Phys.*, 2011, **83**, 195131.
36 S. P. Ong, *et al.*, Python Materials Genomics (pymatgen): A robust, open-source python library for materials analysis, *Comput. Mater. Sci.*, 2013, **68**, 314–319.
37 R. Tran, W. Sun and K. A. Persson, Surface energies ofelemental crystals, *Sci. Data*, 2016, **3**, 1–13.
38 I. Mosquera-Lois, S. R. Kavanagh, A. Walsh and D. O. Scanlon, ShakeNBreak: Navigating the defect configurationallandscape, *J. Open Source Softw.*, 2022, **7**, 4817.
39 W. Tang, E. Sanville and G. Henkelman, A grid-based Bader analysis algorithm without lattice bias, *J. Phys.: Condens. Matter*, 2009, **21**, 084204.
40 B. J. Keene Review of data for the surface tension of pure metals.
41 G. Wulff XXY. Zur Frage der Geschwindigkeit des Wachsthums und der Auflösung der Krystallflächen.

© 2026 The Author(s). Published by the Royal Society of Chemistry

42 D. Gaissmaier, D. Fantauzzi and T. Jacob, First principles studies of self-diffusion processes on metallic lithium surfaces, *J. Chem. Phys.*, 2019, **150**, 041723.
43 Q. Zhao, *et al.*, On the crystallography and reversibility of lithium electrodeposits at ultrahigh capacity, *Nat. Commun.*, 2021, **12**, 6034.
44 J. Becherer, D. Kramer and R. Mönig, The growth mechanism of lithium dendrites and its coupling to mechanical stress, *J. Mater. Chem. A*, 2022, **10**, 5530–5539.
45 K. Tolborg, J. Klarbring, A. M. Ganose and A. Walsh, Free energy predictions for crystal stability and synthesisability, *Digit. Discov.*, 2022, **1**, 586–595.
46 W. Sun, *et al.*, The thermodynamic scale of inorganic crystalline metastability, *Sci. Adv.*, 2016, **2**, e1600225.
47 H. Adenusi, G. A. Chass, S. Passerini, K. V. Tian and G. Chen, Lithium Batteries and the Solid Electrolyte Interphase (SEI)—Progress and Outlook, *Adv. Energy Mater.*, 2023, **13**, 2203307.
48 M. He, R. Guo, G. M. Hobold, H. Gao and B. M. Gallant, The intrinsic behavior of lithium fluoride in solid electrolyte interphases on lithium, *Proc. Natl. Acad. Sci. U. S. A.*, 2020, **117**, 73–79.
49 Y. Zhou, Y. Huang, Y. Wu, J. Li and Z. Hong, Uncertainty qualification of surface diffusion barriers on lithium metal surface through multiscale simulations, *J. Power Sources*, 2025, **630**, 236181.
50 J. X. K. Zheng, J. Yin, T. Tang and L. A. Archer, Moss-like Growth of Metal Electrodes: On the Role of Competing faradaic Reactions and Fast Charging, *ACS Energy Lett.*, 2023, **8**, 2113–2121.
51 S. T. Oyakhire and S. F. Bent, Interfacial engineering of lithium metal anodes: what is left to uncover?, *Energy Adv.*, 2024, **3**, 108–122.

© 2026 The Author(s). Published by the Royal Society of Chemistry